Chemical Engineering Research and Design 206 (2024) 226–241

Contents lists available at ScienceDirect

Chemical Engineering Research and Design

journal homepage: www.elsevier.com/locate/cherd

A draft tube to improve mixing in swirling flow-based solid–liquid mixing reactors

Zhu Yang [a], Thomas Holemans [a], Bert Lagrain [b], Bert Sels [b], Maarten Vanierschot [a,c,*]

[a] Department of Mechanical Engineering, Group T Leuven campus, KU Leuven, Leuven, B-3000, Belgium
[b] Department of Microbial and Molecular Systems, KU Leuven, Leuven, B-3000, Belgium
[c] Material Science, Innovation and Modelling (MaSIM), North-West University, Mmabatho, 2745, South Africa

ARTICLE INFO

Keywords:
Swirl Flow Reactor
Solid–liquid mixing
Draft tube
Coanda effect
Computational Fluid Dynamics
Coherent structure identification

ABSTRACT

The Swirl Flow Reactor (SFR) is a recently proposed specially designed reactor to address challenges of solid–liquid mixing for high-temperature and high-pressure processes. Previous research has shown that the mixing homogeneity of the SFR is not yet optimal and has still potential for improvement. To enhance the homogeneity of the SFR and to optimize the utilization of the previously identified Precessing Vortex Core at the nozzle, an improvement is proposed by the inclusion of a draft tube in the reactor center. Computational Fluid Dynamics is used to study the flow structure, particle distribution, and large-scale coherent structures in the SFR. The improved SFR has been validated for its more homogeneous mixing, where the homogeneity is improved from 0.945 for the original reactor to 0.991 in the new proposed design. Also, the influence of the draft tube on the fluctuating velocities and turbulence within the improved SFR has been indicated. In addition, Spectral Proper Orthogonal Decomposition (SPOD) is used to identify and reconstruct the coherent structures in the reactor. A flattened double-layer helical precessing vortex core (PVC) and its second-order harmonic at frequencies of 35.8 Hz and 71 Hz have been identified, which introduce extra large scale mixing near the nozzle of the reactor.

1. Introduction

In the chemical industry, solid–liquid mixing plays a significant role, where solid particles are suspended in a turbulent flow to enhance both solid–liquid heat and mass transfer (Shi and Rzehak, 2020). This is extensively applied in various operations, including catalytic reactions, hydrogenation, crystallization, leaching, and precipitation (Carletti et al., 2014). Among the numerous available mixing technologies, the mechanically stirred tank is the most commonly used technique for solid–liquid mixing (Yao et al., 2023). After years of exploration and research, the energy and economic efficiency of mechanically stirred tank reactors (STRs) have been greatly improved (Jaszczur and Młynarczykowska, 2020). These studies focus on exploring and improving the effects of various key variables associated with mechanically stirred tanks, such as impeller rotational speed, power consumption (Mishra and Ein-Mozaffari, 2017), impeller structure (Gu et al., 2017; Kazemzadeh et al., 2020; Dang et al., 2022; Tamburini et al., 2014), and baffle adjustments. The effect of the inclusion of a draft tube on the fluctuating velocities and turbulence in the STR was also recorded and analyzed (Wang et al., 2022). However, these improvements have not altered the fundamental structure of STRs, as the rotating component's sealant is still vulnerable to leaks, wear, and friction (Drago and Tones, 2009). In industrial-scale applications, achieving reliable bearing seals under high-temperature and high-pressure conditions represents a significant challenge. The industrial sector has numerous reports on the failure of high-pressure vessel seals, resulting in risks to both infrastructure and the environment (Shah, 1991; Pangarkar, 2017). In addition, a mechanically agitated vessel demands a large power input to provide adequate mixing, especially for substances with a high viscosity (Shah, 1991; Wang et al., 2012). For solid–liquid mixing, the viscosity of solid–liquid suspensions tends to increase substantially as the concentration of solid particles rises (Chen and Li, 2020). This limits the fill rate of the feedstock in the reactor and limits the yield per reactor volume, which undoubtedly increases the cost of industrial production. Owing to the absence of industrial-scale techniques for solid–liquid mixing under high-temperature and high-pressure conditions, many promising new technologies encounter limitations in their application towards industrial production volumes.

Recently, a solid–liquid mixing technology based on swirling flow, named Swirl Flow Reactor (SFR), has been proposed to address the

* Corresponding author at: Department of Mechanical Engineering, Group T Leuven campus, KU Leuven, Leuven, B-3000, Belgium.
E-mail address: maarten.vanierschot@kuleuven.be (M. Vanierschot).

https://doi.org/10.1016/j.cherd.2024.05.005
Received 11 January 2024; Received in revised form 24 April 2024; Accepted 2 May 2024
Available online 8 May 2024
0263-8762/© 2024 Institution of Chemical Engineers. Published by Elsevier Ltd. All rights reserved.

urgent need for industrial-scale implementation in the Reductive Catalytic Fractionation (RCF) of the lignocellulose sector (Yang et al., 2023b). This sector is unable to reach industrial production levels due to the absence of solid–liquid mixing technologies capable of operating under high-temperature (180–250 ° C) and high-pressure (50–130 bar) conditions with high solid concentrations up to 20 vol% (Renders et al., 2019; Cooreman et al., 2020). RCF of lignocellulose is a promising technology for directly converting biomass into small-molecule chemical feedstocks (Renders et al., 2018, 2019). Upon assessing the economic and environmental viability of this technology, they concluded that the added value of lignin valorization is significant (Van den Bosch et al., 2015). However, the largest reported mechanically stirred batch reactor for RCF is a 50 L pilot-scale set-up with a solid loading up to 6 $wt\%$ (Renders et al., 2018, 2019). Such a reactor falls short of meeting the requirements of industrial production and is economically infeasible (Tschulkow et al., 2020). In addition, magnetic drive mixers, as widely employed leak-proof industrial mixing devices, could supply the requisite torque for adequate mixing in both laboratory-scale and pilot-scale RCF reactors (Van den Bosch et al., 2015). However, from both technical and financial standpoints, magnetic drive mixers are not viable for industrial-scale applications. This limitation arises because the viscosity of the suspension inside the reactor cannot be exceedingly high as the torques transmitted by magnetic drive mixers are not as large as those conveyed by mechanically connected shafts (Cooreman et al., 2020). In lab- and pilot-scale reactors for RCF, this technology is able to operate at a solid loading up to 25wt% (Cooreman et al., 2020). In the context of a lack of suitable mixing technologies, the introduction of the SFR not only facilitates the industrialization of the RCF of lignocellulose biorefinery, it also provides new opportunities for solid–liquid mixing at industrial scale for high-temperature and high-pressure conditions. Technologies that could potentially benefit from the utilization of the SFR include hydrothermal synthesis of nanoparticles (Cao and Wang, 2011), direct coal liquefaction (Fratczak et al., 2018), and hydrothermal carbonization (Hoekman et al., 2011), among others. Therefore, further research and improvements on the SFR are both necessary and meaningful.

SFR is a mixing technique that utilizes swirling flow, also known as vortex flow. Swirling flows, commonly observed in nature and various technical equipments, possess unique capabilities for enhancing mixing, separation (Gupta et al., 1984), and stabilization, and it have shown excellent performance in various fields such as combustors, fluidized bed reactors, and micro-scale reactors (Vanierschot and Van den Bulck, 2007a; Ogus et al., 2018; Kuzmin, 2021). The SFR employs a unique fluid dynamics approach to achieve solid–liquid mixing. A swirl jet is injected into the reactor from the bottom, and evolves into a Coanda Jet Flow (CoJF), generating a spiraling upward flow along the reactor wall. Due to the annular outlet/filter design, the liquid in the center top area is largely stationary. After being blocked by the filter, the solid particles descend by gravity from the middle region, and they are dispersed by the strong fluctuations generated by the CoJF at the bottom, after which they join the updraft along the wall again. This process forms an axial recirculation, and the intense fluctuations generated by the shear flow and recirculatory currents augment mixing and facilitate chemical reactions. The SFR eliminates the need for stirring impellers and relies on fixed sealing, making it a safer and more economical option for extreme working conditions. In addition, the SFR is a jet-based flow-through solution, which allows for enhanced heat transfer capabilities, as it enables the integration of a heat exchanger in the external loop. This design configuration facilitates nearly isothermal operation, leading to a uniform temperature distribution that contributes to its overall performance and efficiency, in contrast to mechanically stirred tanks, which may encounter limitations at industrial scales due to restricted jacket areas and impaired temperature control caused by cooling coils (Pangarkar, 2017).

The flow structure, particle distribution, and large-scale coherent structures inside the SFR are discussed in the work of Yang et al. (2023b). The SFR shows a satisfactory degree of mixing. However, the particle concentration distribution in the reactor was not perfect: the average particle distribution in the vessel is 20 vol%, where the lowest concentration is 14% on the side near the nozzle, while the highest concentration is 27% on the side near the outlet. This inhomogeneity is caused by a poor return of particles in the axial direction at the center, despite the persistent negative axial velocity observed in the central region of the vessel. However, a substantial amount of fluctuating velocity is present and accompanied by a continuous capture of particles by the outer upward jet, and particles are incorporated into the flow again. Therefore, from the top to the bottom, the sinking of particles gradually diminishes, resulting in a decrease in the number of particles involved in the axial particle circulation. The existence of a Precessing Vortex Core (PVC) at the nozzle of the SFR presents a valuable opportunity for the effective dispersion of particles and enhancement of reaction processes. However, the inability of certain particles to return smoothly to the nozzle region hinders the full utilization of the PVC's potential. To enhance the homogeneity of the SFR and to optimize the utilization of the PVC at the nozzle, an improved solution using a draft tube in the center of the vessel could be implemented. Draft tubes are basically tubes or shells installed within mixing vessels, which find applications in various mixing operations (Coker, 2007). These components serve to influence the flow dynamics within the reactor, thereby impacting mixing efficiency and reaction kinetics. The incorporation of stretching tubes can be particularly valuable for optimizing fluid and particle interactions in complex systems. In mechanically stirred tanks, the draft tube is mounted around the shaft of the mixer including the usual axial impeller, which allows a special or top-to-bottom fixed flow pattern to be set up in the fluid system (Coker, 2007). This improves mixing efficiency and can prevent short-circuiting of liquid from the inlet to the outlet in a continuously stirred tank. Based on a similar principle, this improvement in the SFR is aimed at physically separating the central downward flow from the outer upward flow to ensure that all particles are returned to the nozzle side from the top and complete the full extent of the axial particle circulation. In addition, the draft tube only guides the flow, it is not subjected to forces as a structural element. This improvement is straightforward from a manufacturing point of view, as the draft tube can be welded to the ring filter support of the original design and installed in the same position. As such, this improvement is stable, cheap, and reliable.

To verify this idea, a Computational Fluid Dynamics (CFD) model is established for this improved design of the SFR to explore the complex solid–liquid suspension problem. The particular challenge posed by this study lies in the high concentration of solid particles, constituting 20 vol%, loaded into the mixing vessel. Such elevated levels render many experimental techniques unsuitable for application. This presents an obstacle to the accurate characterization and optimization of mixing and reaction dynamics within the system through experimental methods. Optical-based flow field measurement techniques, including Particle Image Velocimetry (PIV) and Laser Doppler Velocimetry (LDV), are widely used for investigations in flow fields (Wiederseiner et al., 2011; Wright et al., 2017). However, the clarity of these techniques is compromised due to the medium turbidity from high particle suspensions (Wright et al., 2017). Additionally, Nuclear Magnetic Resonance and Refractive Index Matching are not applicable in this reactor design due to their prohibitive cost and rigorous implementation requirements (Wiederseiner et al., 2011). Lastly, Ultrasound Imaging Velocimetry (UIV or echo-PIV), has gained prominence in the last decade, offering better insights into flows that optical measurements cannot access (Shukla and Prakash, 2006; Poelma, 2016). However, UIV is primarily utilized for cardiovascular flows, but its efficacy in reactor scales and intricate two-phase flows warrants further exploration (Poelma, 2016). Due to the paucity of fitting experimental techniques, Computational Fluid Dynamics has emerged as a pivotal tool for visualizing flow structures in a solid–liquid swirl mixing vessel.

For the complex flow field of a SFR, turbulence-induced dynamic fluctuations also play a significant role in the solid–liquid mixing process. The Reynolds-averaged Navier–Stokes (RANS) models are frequently employed for complex geometries (Maluta et al., 2019), due to their favorable computational credibility and relatively manageable computational cost. The standard $k-\varepsilon$ model (Launder and Spalding, 1974) is predominant in simulating stirred tank solid–liquid mixing in the early stages (Kasat et al., 2008; Min and Gao, 2006; Wang et al., 2006). However, modified models like the renormalization group (RNG) $k-\varepsilon$ model (Yakhot and Orszag, 1986) and realizable $k-\varepsilon$ model (Shih et al., 1995) offer enhanced accuracy in certain conditions (Liu et al., 2019; Li et al., 2015). The RNG $k-\varepsilon$ model achieves the best prediction accuracy in the comparison of various models with experimental measurements (Xu et al., 2021). Besides, this study's focus on solid–liquid mixing inherently involves two-phase flows, making it essential to explore the dynamics of solid particle suspension. This exploration hinges on comprehending solid–solid and solid–liquid interactions. Two primary methods to model solid–liquid suspension processes exist: Eulerian–Lagrangian (E–L) and Eulerian–Eulerian (E–E) approaches (Peker and Helvaci, 2008). The E–E methods visualize the dispersed particle phase as a continuous fluid that interacts and interpenetrates with the liquid phase (Gidaspow, 1994), where separate continuity equation and momentum equations are solved for both phases with a shared pressure. This method has found favor with many researchers for dense systems (Shi and Rzehak, 2020; Xu et al., 2021; Montante and Magelli, 2007). However, the E–E approach can encounter discrepancies in dense systems with average particle concentrations of 20 vol% due to pronounced solid–solid interactions (Wadnerkar et al., 2012). To address this, Gidaspow (1994) introduced the kinetic theory of granular flow (KTGF) model. Combining the E–E approach with the KTGF model (EE-KTGF) yields accurate predictions for particle distribution in dense systems, aligning well with experimental data (Xu et al., 2021; Wadnerkar et al., 2016). Conversely, the E–L method is not appropriate for this study, as solid phases are considered as distinct entities, limiting their applicability to low particle concentrations (Mishra and Ein-Mozaffari, 2017). This study leverages both the RNG model and the EE-KTGF model, and their combined efficacy is validated against experimental measurements in the literature (Xu et al., 2021; Wang et al., 2022; Xie and Luo, 2018). Moreover, to simulate the particle filter's function, a macro-scale porous medium model is utilized, effectively reducing computational load, as validated in several investigations (Hrouda et al., 2021; Fotovati et al., 2012).

This study establishes a CFD model for the modified SFR with a draft tube to explore the complex solid–liquid mixing. The time-averaged velocity fields and particle volume fraction fields are analyzed to study the flow structure and assessment of the mixing efficiency after the modification. In addition, the effect of the inclusion of a draft tube on the fluctuating velocities and turbulence in the SFR is also recorded and analyzed. Moreover, the highly dynamic transient flow fields are also captured and SPOD is conducted on these flow fields to identify and study the evolution of the large-scale coherent structures (Sieber et al., 2016). In addition, this study contrasts the flow characteristics between the modified SFR and its original configuration, elucidating the mechanisms behind the enhanced mixing effect achieved by draft tube, and investigates the influence of this modification on the overall flow structure.

2. Mathematical model

2.1. Turbulence model

The $k-\varepsilon$ model, grounded in the Reynolds-averaged Navier–Stokes (RANS) paradigm, holds significant relevance for the forecasting of turbulent flow fields. Within this model, the turbulent viscosity, μ_t, is derived through the transport equations for the turbulent kinetic energy k and its dissipation rate ε (Launder and Spalding, 1974). A variant of this model, the RNG $k-\varepsilon$, incorporates modifications via the renormalization group (RNG) methodology. This adaptation provides a superior response to rapidly strained flows, such at swirling flows with a high swirl number (Yakhot and Orszag, 1986). The modified transport equations are shown as Eqs. (1) and (2):

$$\frac{\partial}{\partial t}(\rho k)+\frac{\partial}{\partial x_i}(\rho k u_i)=\frac{\partial}{\partial x_j}\left(\alpha_k \mu_{eff}\frac{\partial k}{\partial x_j}\right)+G_k-\rho\varepsilon, \tag{1}$$

$$\frac{\partial}{\partial t}(\rho \varepsilon)+\frac{\partial}{\partial x_i}(\rho \varepsilon u_i)=\frac{\partial}{\partial x_j}\left(\alpha_\varepsilon \mu_{eff}\frac{\partial \varepsilon}{\partial x_j}\right)+C_{1\varepsilon}\frac{\varepsilon}{k}G_k-C_{2\varepsilon}\rho\frac{\varepsilon^2}{k}-R_\varepsilon, \tag{2}$$

where $C_{1\varepsilon}$ and $C_{2\varepsilon}$ are constants ($C_{1\varepsilon}$=1.42, $C_{2\varepsilon}$=1.68). μ_{eff} is the effective viscosity and G_k is the generation of turbulent kinetic energy due to the mean velocity gradients. R_ε is an additional term in the RNG $k-\varepsilon$ model compared to the standard $k-\varepsilon$ model, which improves the responsiveness to the effects of rapid strain and streamlines curvature (Ansys, 2019).

2.2. Multi-phase model

The Two-Fluid Model (TFM) applied in this study is the Eulerian–Eulerian (E–E) model, which provides a framework for simulating solid–liquid suspension flows, and is a good candidate for simulating the SFR. For each phase, both continuity and momentum equations are addressed. The turbulent fluctuations' effects on velocities and scalar quantities for the solid phase are modeled using the $k-\varepsilon$ dispersed turbulence model. Besides, the RNG $k-\varepsilon$ model forecasts the turbulent predictions for the primary phase. Turbulent predictions for the dispersed phase are obtained through Tchen's theory on the dispersion of discrete particles (Hinze, 1975), which prioritizes time and length scales for evaluating turbulent quantities. As mass transfer between phases is not considered in this study, the mass continuity equation for phase q is

$$\frac{\partial}{\partial t}\left(\alpha_q\rho_q\right)+\nabla\left(\alpha_q\rho_q\vec{u}_q\right)=0, \tag{3}$$

where ρ is the density, $\vec{u}$ the velocity vector, and α the volume fraction. The momentum equations for the liquid phase l and solid phase s are as follows:

$$\begin{aligned}&\frac{\partial}{\partial t}\left(\alpha_l\rho_l\vec{u}_l\right)+\nabla\left(\alpha_l\rho_l\vec{u}_l\vec{u}_l\right)=\\&-\alpha_l\nabla P+\nabla\bar{\bar{\tau}}_l+\alpha_l\rho_l\vec{g}+\vec{R}_{ls}+\left(\vec{F}_{tb.l}+\vec{F}_{B.l}+\vec{F}_{Lift.l}+\vec{F}_{Vm.l}\right)+S_l,\end{aligned} \tag{4}$$

$$\begin{aligned}&\frac{\partial}{\partial t}\left(\alpha_s\rho_s\vec{u}_s\right)+\nabla\left(\alpha_s\rho_s\vec{u}_s\vec{u}_s\right)=\\&-\alpha_s\nabla P-\nabla P_s+\nabla\bar{\bar{\tau}}_s+\alpha_s\rho_s\vec{g}-\vec{R}_{ls}+\left(\vec{F}_{tb.s}+\vec{F}_{B.s}+\vec{F}_{Lift.s}+\vec{F}_{Vm.s}\right)+S_s,\end{aligned} \tag{5}$$

where $\vec{g}$ is the gravitational acceleration, P is the pressure shared by all phases and P_s is the solid pressure, $\bar{\bar{\tau}}$ is Reynolds stress–strain tensor and $\vec{R}_{ls}$ is the interaction force between phases. $\vec{F}_{tb}$, $\vec{F}_B$, $\vec{F}_{Lift}$, and $\vec{F}_{Vm}$ are the effect of turbulent dispersion force, buoyancy force, lift force, and virtual mass force, respectively. Furthermore, the Kinetic Theory of Granular Flow (KTGF) model predicts collisions amongst solid particles. Detailed discussions on this are available in the ANSYS Fluent Theory Guide (Ansys, 2019). Besides, the interaction force $\vec{R}_{ls}$ represents as:

$$\sum_{p=1}^{n}\vec{R}_{ls}=\sum_{p=1}^{n}K_{ls}\left(\vec{u}_l-\vec{u}_s\right), \tag{6}$$

and

$$\sum_{p=1}^{n}\vec{R}_{sl}=\sum_{p=1}^{n}K_{sl}\left(\vec{u}_s-\vec{u}_l\right). \tag{7}$$

In this research, the Huilin–Gidaspow drag force model is utilized to obtain the interphase momentum exchange coefficient K_{ls} ($K_{ls}=K_{sl}$),

which offers a smooth transition mechanism when solid volume fractions are less than 20 vol% (Huilin and Gidaspow, 2003). Wadnerkar's research compared experimental and numerical data for an average volume fraction nearing 20% and found reasonable alignment between both. The expression of the switching function of the Huilin–Gidaspow model is given as:

$$K_{sl} = \psi K_{sl-Ergun} + (1-\psi) K_{sl-Wen\&Yu}, \tag{8}$$

where the stitching function is of the form

$$\psi = \frac{1}{2} + \frac{tan^{-1}\left(262.5\left(\alpha_s - 0.2\right)\right)}{\pi}. \tag{9}$$

$K_{sl-Wen\&Yu}$ and $K_{sl-Ergun}$ are obtained by the Wen-Yu equation and the Ergun equation, which is given as:

$$K_{sl-Wen\&Yu} = \frac{3}{4} C_D \frac{\alpha_s \alpha_l \rho_l \left|\vec{u}_s - \vec{u}_l\right|}{d_l} \alpha_l^{-2.65}, \tag{10}$$

where

$$C_D = \frac{24}{\alpha_l Re_s}\left[1 + 0.15\left(\alpha_l Re_s\right)^{0.687}\right], \tag{11}$$

and

$$Re_s = \frac{\rho_l d_s \left|\vec{u}_s - \vec{u}_l\right|}{\mu_l}. \tag{12}$$

The Ergun equation is of the form:

$$K_{sl-Ergun} = 150 \frac{\alpha_s \left(1-\alpha_l\right)\mu_l}{\alpha_l d_s^2} + 1.75 \frac{\rho_l \alpha_s \left|\vec{u}_s - \vec{u}_l\right|}{d_s}. \tag{13}$$

Additionally, the turbulent dispersion force indicates inter-phase turbulent momentum transfer between solid and liquid phases, especially when turbulent eddies surpass particle sizes (Xu et al., 2021). Given the enhancement in dense solid–liquid mixing predictions by both the Burns and Simonin models (Xu et al., 2021), the Burns model is employed in this study. Furthermore, as the Basset force is substantially less than the drag force (Yang and Mao, 2014), and given the negligible nature of lift forces, these forces are excluded in correspondence with various other studies (Liu et al., 2023; Xu et al., 2021; Sardeshpande et al., 2011; Tamburini et al., 2014). Finally, the virtual mass force is only significant when the mass of the second phase is significantly smaller than the one of the first phase, so it is not accounted for in this study.

2.3. Porous medium model

The filter's functionality is captured through a porous media model, which provides computational efficiency over intricate filter structures. This model introduces an added momentum source term in the canonical momentum equations to express the resistance of the filter. For a homogeneous porous medium, the source term, S_{porous}, is defined as

$$S_{porous} = \left(C_{vr}\mu u_i + C_{ir}\frac{1}{2}|u|\,u_i\right), \tag{14}$$

wherein, C_{vr} signifies the viscosity resistance factor, and C_{ir} stands for the inertial resistance factor. The viscosity resistance factor, C_{vr}, denotes the loss coefficient in proportion to the velocity, while the inertial resistance factor, C_{ir}, signifies the loss coefficient along the directional axis of the flow. In the SFR, an efficient filter ensures that the fluid phase can permeate the filter region while hindering the solid phase. To obtain this behavior, a substantial inertial resistance, C_{ir}, is imposed on the solid phase.

3. Computational domain and numerical methods

In the numerical model, the implementation of the swirl-generating device was crucial due to its significant impact on the flow structures. A radial-type swirl generator was utilized in this study, the same as the one in the work of Yang et al. (2023b) and it is shown in Fig. 1a. This device utilizes guide vanes that introduce the fluid tangentially into the main channel, effectively creating a swirling jet. Once the fluid passes through the swirl generator and acquires a rotational motion, it is directed into a circular inlet tube with a diameter of D_o = 22.5 mm and a length of $1.4D_o$. Subsequently, the swirling jet emerges into the primary section of the SFR through a specifically designed nozzle. Fig. 1 illustrates a cross-sectional view of the nozzle in the $x-z$ plane with its dimensional details. The main body of the SFR is cylindrical, with an annular filter at the outlet to keep particles inside the reactor, modeled as a porous medium. The length and diameter of the cylindrical main body are $9.2D_o$ and $4.9D_o$, respectively. The inner and outer diameters of the annular filter and outlet are $3.3D_o$ and $4.9D_o$, respectively. These dimensions were determined by a parametric analysis in the work of Yang (2023). The dimensions of the additional draft tube in the reactor are also shown in Fig. 1b. Furthermore, the dimensions of the nozzle have been adjusted and adapted based on the design used in combustors in the work of Vanierschot and Van den Bulck (2007b). In this adaptation, the bottom surface of the main body has been altered to include a 15-degree inclination. This modification facilitates the nozzle to generate a CoJF. The reference origin point of the coordinate system is positioned at the central axis, aligned with the bottom of the side wall surface.

The computational grid is generated using a hexahedral multi-block approach. All grid cells meet the minimal requirements for aspect ratio, non-orthogonality, growth ratio, and skewness. Fig. 2a shows an overview of the computational grid, Fig. 2b gives a detailed view of the grid of the porous medium and draft tube, and Fig. 2c gives a detailed view of the grid of the swirl generator and inlet tube. The no-slip velocity wall condition is rigorously imposed on all walls. In addition, scalable wall functions are implemented for turbulence treatment in the near-wall region, due to the great variation of $y^\star$ values in the near-wall mesh caused by the intricate and dynamic fluctuating flow within the vessel and the compact nature of the swirl generator. The maximum $y^\star$ value is about 278 at the swirl generator, and the minimum $y^\star$ value is about 4 at the cylindrical wall surface of the main body. Scalable wall functions are applied to prevent the degradation of standard wall functions when applying a grid refinement for $y^\star$ values below 11, which ensures the credibility of the prediction of the wall function for $y^\star < 300$ (Ansys, 2019). In addition, a fixed time step of $\triangle t = 5 \times 10^{-4}$ s is applied in the simulation. Each time step was considered converged when the residuals for all transport equations dropped at least 3 decades during the respective time step.

This study employs the commercial computational fluid dynamics code Ansys Fluent V20.1 for the numerical simulations. To obtain the coupled pressure/velocity fields, the phase-coupled SIMPLE (Semi-Implicit Method for Pressure Linked Equations) algorithm is utilized at each time step. The temporal derivative term is discretized using a bounded second-order implicit scheme to ensure accuracy and stability. The least squares cell-based method is employed to evaluate scalar gradients within each cell. Spatial discretization of momentum, volume fraction, turbulent kinetic energy, and turbulent dissipation rate equations is accomplished using the QUICK (Quadratic Upstream Interpolation for Convective Kinematics) scheme. Furthermore, pressure discretization is accomplished using the PRESTO! differencing scheme.

To model the solid–liquid flow in a high-temperature, high-pressure RCF extraction process, methanol at 130 bar pressure and 235 degrees Celsius was used as the governing fluid. These conditions approximate the operating conditions. At those conditions, methanol has a density of 522 kg/m^3 and a kinematic viscosity $\nu = 1.37 \times 10^{-7}$ m$^{2/s}$ (Xiang et al., 2006). The solid phase employed in the simulation represents biomass and is modeled as small spherical particles with a diameter of 0.3 mm. These particles possess a density of 913 kg/m^3 (corresponding to a specific gravity of 1.75) and an average volume fraction of 20 vol% (30.4 wt%). These material properties are summarized in the Table 1. In addition, the direction of gravity is pointed to the negative

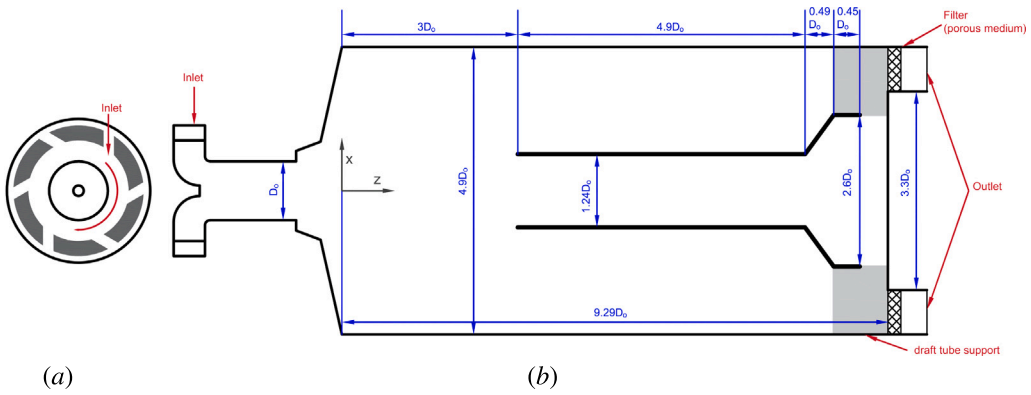

Fig. 1. Schematic view of the improved reactor: (*a*) layout of the swirl generator; (*b*) sketch of the computational flow domain in the x-y plane.

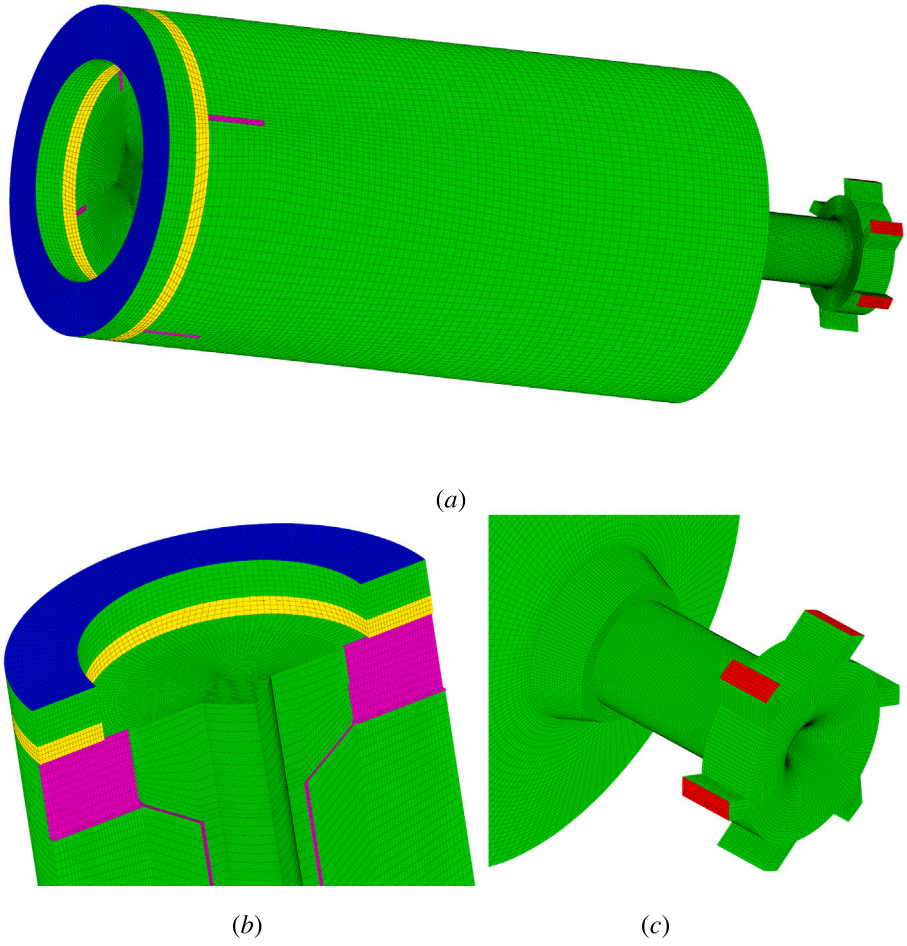

Fig. 2. Layout and computational grid used for the simulation: (*a*) full set-up; (*b*) porous medium and draft tube; (*c*) swirl generator.

direction of the z-axis, i.e. the particles settle on the bottom of the vessel and into the nozzle when stationary. The swirl jet has a flow rate of 18.8 L/min, while the Reynolds number Re is 130,000. Here, the mean axial velocity $u_o = 0.78$ m/s and a nozzle diameter $D_o = 22.5$ mm, are employed to calculate the Reynolds number. To quantify the intensity of the swirling flow, a modified swirl number Sw^* for recirculating flow is utilized (Gyllenram et al., 2006), which is the ratio between the axial flux of tangential momentum and the axial flux of axial momentum divided by the radius. The swirl number Sw^* is computed at a plane $-0.3D_o$ below the end of the inlet tube at $Z = -1.17D_o$, giving $Sw^* = 1.7$.

Table 1
Material properties.

Liquid			Solid		
Density	Viscosity	Flow rate	Density	Diameter	Volume fraction
522 kg/m^3	1.37×10^{-7} m^2/s	18.8 L/min	913 kg/m^3	0.3 mm	20 vol%

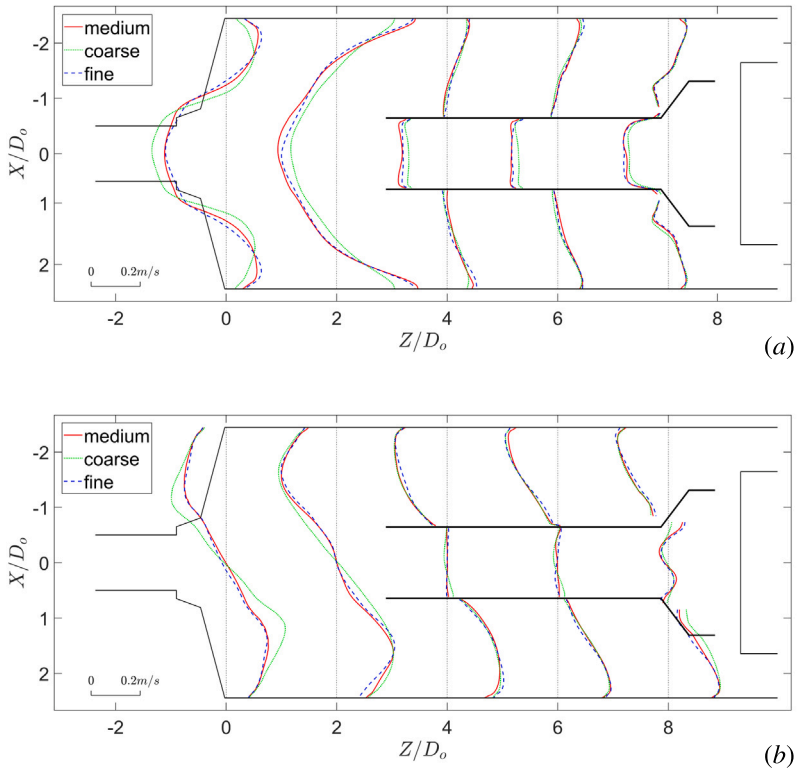

Fig. 3. Radial distribution of time-averaged velocities using three different grids, (*a*) axial velocity; (*b*) tangential velocity.

4. Grid independence study

To obtain an accurate numerical solution, it is essential to account for the resolution of the grid. In order to conduct a grid-independence test, three distinct grids were used: a coarse grid with 0.67×10^6 cells, a medium grid with 1.66×10^6 cells, and a fine grid with 3.46×10^6 cells. The grid size was uniformly scaled in all directions for each of these grids. Here a single-phase flow simulation was performed with an identical Reynolds number, while maintaining the same numerical configuration to verify grid independency. Due to the extensive computational resources required for multiphase flow simulations, achieving axisymmetric time-averaged results for the improved Swirling Flow Reactor (SFR) with low-frequency flow structures poses a time-consuming task. In our case, the computational time for a medium grid, two-phase simulation exceeded two months, even when employing a 216-core cluster. Pursuing such simulations with the fine grid is very impracticable, as it is neither cost- nor time efficient. Moreover, since the liquid phase plays a dominant role in the mixing, its influence on the overall outcome is substantial. A comparative analysis of the flow variable gradients in both single-phase and two-phase medium-grid simulations reveals a high degree of similarity (not shown in this paper), and hence the discretization error should also be similar, thereby validating our approach. Further corroborating this, several other studies have also employed the single-phase approach to validate grid independence of multiphase simulations (Shi and Rzehak, 2020; Wadnerkar et al., 2012; Yang et al., 2023b). Given these constraints and justifications, the use of a single-phase flow simulation to validate the discretization error provides a viable path for the computational study of the improved SFR. The profiles of the mean axial velocity and the mean tangential velocity along the radial direction at varying heights are shown in Fig. 3. In the presented profiles, the medium and fine meshes exhibit high proximity, whereas noticeable disparities are observed in the coarse mesh. The primary distinctions between the coarse, medium, and fine meshes manifest predominantly in the nozzle region, while on the outlet side, the three meshes demonstrate nearly identical characteristics. This observation suggests that the coarse mesh is relatively inadequate in capturing the Coanda flow near the nozzle outlet, resulting in discernible variations compared to the more refined meshes. In addition, for the maximum mean axial velocity and maximum mean tangential velocity in the entire computational domain, the deviations between medium and fine grids are 0.5% and 0.05%, respectively, while the deviation between medium and coarse grids are 2.6% and 0.7%, respectively. It is evident that the medium and fine grids have more similar results, while the resolution of the coarse grid exhibits a deficiency in accuracy in predicting the jet flow pattern. Considering both computational cost and accuracy, the medium mesh (1.66×10^6 cells) is used for the two-phase flow simulations.

Due to the operating conditions of the methanol present in the SFR, namely a temperature of 235 degrees Celsius and a pressure of 130 bars, obtaining measurements of the concentration and velocity field poses practical challenges. The lack of optical access and the thick insulation necessary to maintain the reactor at a sufficiently high temperature hinder the feasibility of such measurements. Additionally, the high concentration of particles in the flow results in significant turbidity, rendering traditional laser-based velocity measurement techniques like LDA (Laser Doppler Anemometry) and PIV (Particle Image Velocimetry) unviable. Consequently, PIV measurements were conducted in a one-phase flow within a transparent reactor, without a draft tube, operating at the same swirl number as the simulation case, which reveals that the Coanda jet can also be found in the experiments, validating the numerical simulations' flow pattern and turbulence model (Yang et al., 2023b).

5. Mean particle distribution

Since a draft tube is included, the particles can be confined to the center of the reactor and sink to the nozzle side. This greatly improves the particle distribution along the axial direction. Fig. 4 shows the contours of the time-averaged particle volume fraction in a plane

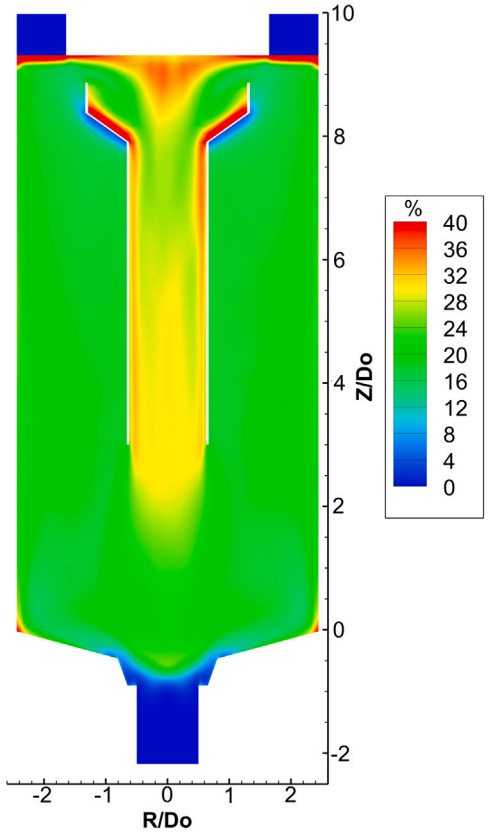

Fig. 4. Time-averaged particle volume fraction field in a plane tilted 45 degrees in the tangential direction.

tilted 45 degrees in the tangential direction to show the details in the area covered by the support of the draft tube, where R is the radius. The particles in the vessel show a uniform distribution, which shows a consistent particle volume fraction from the bottom to the top. However, as a result of the filtering, there is a 3 mm thick region of dense particles in front of the filter, where the volume fraction is up to 40%. This region is also present in the original design, and the volume fraction of particles that accumulate in the improved design is 15% lower compared to the original one. In addition, Fig. 5 shows the axial distribution curve of the particle concentration. The blue line is the mean particle volume fraction in different cross sections along the axial direction of the improved design. For reference, the red dotted line represents the original design, and the yellow dashed line is the average particle volume fraction of the reactor (20 vol%). Apart from the dense particle area in front of the filter, the particle volume fractions of this improved design remain in the range of $20-2$ v% and $20+2$ v%, which is a noticeable improvement over the range of $20-6$ v% and $20+7$ v% of the original design (Yang et al., 2023b). From $Z/D_o = 0$ to $Z/D_o = 9.2$, 104 equally spaced $X-Y$ planes were sampled, giving a homogeneity of 0.991, where the homogeneity of the original design is 0.945 (Yang et al., 2023b). Hence, the improved SFR shows a remarkably improved mixing performance.

6. Mean velocity fields

Figs. 6a and b show the distribution of the liquid and particle velocity averaged over time in a plane tilted 45 degrees in the tangential direction to avoid shading of the support of the duct center. The uniform velocity vectors indicate flow directions, while the contours represent the magnitude of the in-plane velocity components. As shown in Fig. 6, the liquid phase has the same flow structure as the particle phase, while the particle phase has an axial velocity that is 0.02 m/s lower than the liquid phase. This difference in velocity is required to generate sufficient drag force to counteract gravity to maintain a suspension. The Coanda Jet Flow (CoJF) is formed by the swirling jet, which attaches to the outlet wall of the nozzle, driven by the Coanda effect (Vanierschot and Van den Bulck, 2007a). The Coanda flow fully remains until a height of $Z/D_o = 3$, after which only a portion retains its attachment to the wall and flows from the outside of the draft tube to the outlet, while the other portion returns to the nozzle. The occurrence of back-flow can be attributed to the presence of a low pressure in the central region of the swirling flow. At a height of $Z/D_o = 1$, the combined effect of back-flow and the Coanda Jet Flow (CoJF) results in two distinct recirculation zones. Recirculation regions within the vessel facilitate an elongated residence time, thus increasing the mixing efficiency between the two distinct phases (Syred, 2006). Furthermore, the improved design separates the central back-flow from the outer upward flow by the draft tube, allowing for a significant increase in the velocity of the downward flow. As a uniform negative velocity appears in the draft tube, particles can sink from the top to the bottom, and a low pressure is generated inside the draft tube. The pressure in the tube at a height of $Z/D_o = 8$ is 30 Pa lower than in the central area of the top. This pressure difference makes the back-flow of particles in the top central area to be no longer driven by gravity alone, which reduces particle accumulation and promotes the return of accumulated particles in front of the filter. This is also shown in the particle volume fraction curve in Fig. 5. Additionally, because of the physical separation of the outer upward flow from the central downward flow, shear stresses formed between the central descending flow and the outer ascending flow in the original design do not arise. Because the draft tube protects the central particles, it does not come into contact with the outer upward flow during the sinking process. The particles can be transported from the annular outlet to the inlet nozzle. The improved design avoids particles being prematurely captured by the outer upward flow in the middle and upper regions, where some particles do not sink to the nozzle side and cause an uneven distribution of particles in the axial direction. This improvement can also be observed in Fig. 5.

Fig. 7a shows the mean liquid tangential velocity in a plane tilted 45 degrees in the tangential direction. The draft tube has a different direction of rotation inside and outside. Upon exiting the draft tube, the reverse rotating downward flow comes into contact with the external Coanda jet. The rotational and axial flow in opposing directions generates a shear flow characterized by pronounced velocity fluctuations within the central region of the vessel, i.e. $Z/D_o \leq 3$, which is also shown in the RMS contours of the velocity magnitude, as shown in Fig. 7b. In the lower part of the vessel, there are noticeably greater velocity fluctuations than in the middle and upper regions, which are conducive to solid–liquid suspension and facilitate a single reaction. Furthermore, the RMS velocity in the nozzle region at $Z/D_o \leq -0.5$ is identical to the original design in terms of intensity and distribution. Thus, the large-scale coherent structure found in the nozzle in the improved design is presumably similar to the original design in terms of strength and structure.

Compared to the original design (Yang et al., 2023b), the central draft tube was added in the improved design, separating the central downward flow from the outer upward flow. As such, the shear flow found in the original design is not present, and the strength of its fluctuating velocity is reduced. As there is no shear flow to slow down the upward axial flow, the velocity of that outer upward flow experiences a significant increase. This observation is depicted in the time-averaged axial velocity profiles, illustrated in Fig. 8a, where the blue and dashed lines are the liquid and solid velocity profiles of the improved design, respectively, and the red dotted and dash-dotted lines represent the liquid and solid velocity profiles of the original design. On average, the upward axial velocity of the liquid phase on the outer

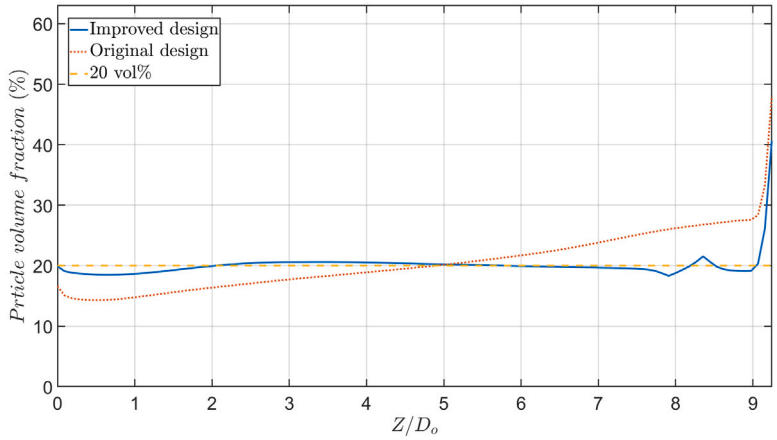

Fig. 5. The distribution of mean particle volume fraction in $X - Y$ planes along the Z axis for the improved and original design (Yang et al., 2023b).

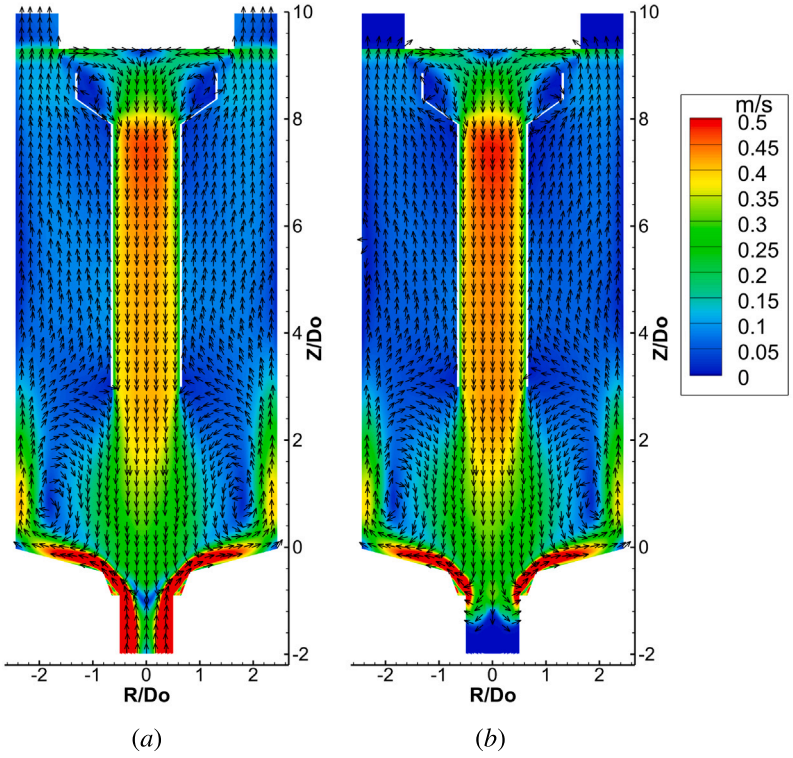

Fig. 6. Time-averaged in-plane velocity field in a plane tilted 45 degrees in the tangential direction: (*a*) liquid phase; (*b*) solid phase.

side of the vessel is found to be 58% higher than the velocity in the original design. On the contrary, the tangential velocity in the improved design shows a reduction compared to the original design, as shown in Fig. 8b, where only the velocity profiles of the liquid phase are shown. As the Stokes number of particles in the body of the vessel is estimated to be $Stk = 0.002$, which is much less than 1, the particles follow the liquid phase with almost the same velocity (Raffel et al., 2018). This phenomenon can be attributed to the presence of the draft tube, which facilitates downward transportation of particles from the upper to the lower region of the reactor. At the same time, the downward flow in the draft tube is not in contact with the outer swirl jet in the upper area until it reaches the bottom, near the nozzle region. The energy of the tangential velocity of the swirling jet is dissipated in the nozzle area by the counter-rotating downward flow, which completes its turn at a height of $Z/D_o = 2$, below which the region has the same direction of rotation as the swirling jet. Because the tangential velocity energy of the swirling jet is dissipated primarily at the bottom region of the vessel, the overall tangential velocity within the system is lower compared to the original design. With lower rotational speeds, the detrimental effects of centrifugal forces can be mitigated, resulting in a reduced incidence of particle adhesion or sinking along the sidewall surface. This advantageous outcome promotes a more uniform distribution of particles within the system. In the original design, the dissipation of tangential velocity energy of the jet occurs primarily in the upper region of the vessel, which is shown in the tangential velocity profile at heights of $Z/D_o = 6$ and 8.

In addition, the kinetic energy of the injected jet flow is the same in the improved design and in the original design, and the pressure drop between the inlet and outlet is almost identical. The proportion of energy accounted for by the mean velocity increases, and the corresponding proportion of energy accounted for by the fluctuating velocity will decrease. Due to the use of a RANS model, small-scale

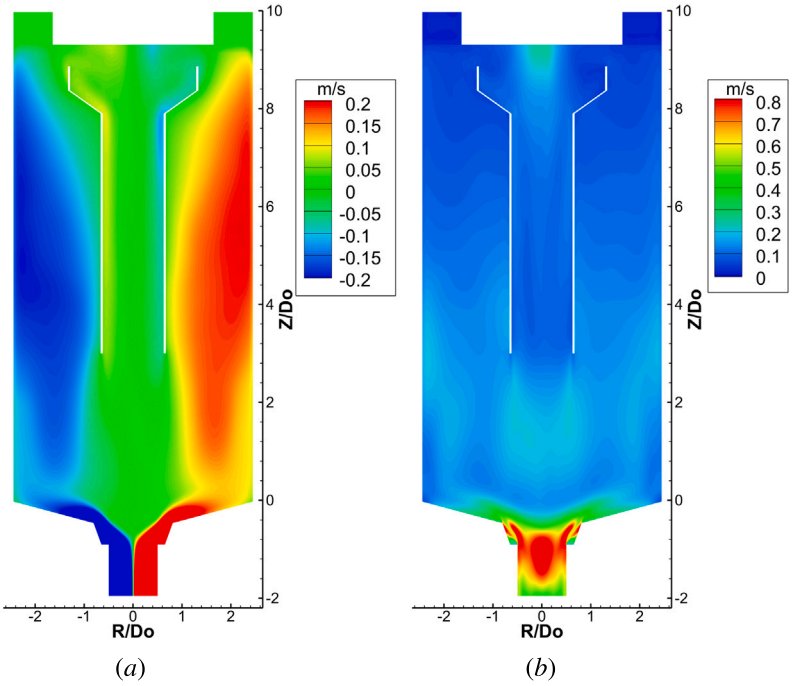

Fig. 7. (*a*) Time-averaged tangential velocity field of the liquid; (*b*) root mean square of the velocity magnitude of the liquid.

turbulent velocity fluctuations are presented in the turbulent kinetic energy (k), and larger-scale fluctuating velocities are solved directly, here represented by the root mean square (RMS) velocity. The RMS velocity profiles and turbulent kinetic energy (k) profiles are shown in Figs. 9a and b, respectively. It should be noted that k discussed in this context represents an additional term used to calculate the Reynolds stress necessary for the closure of the RANS equations. This turbulent kinetic energy is not the actual physical turbulent kinetic energy. However, it has a significant contribution in determining the effect on solid–liquid suspensions or chemical reactions. As shown in Figs. 9a and b, in the lower section of the vessel, specifically below $Z/D_o = 4$, the RMS velocity and turbulent kinetic energy exhibit slightly higher values in the original design compared to the improved design, with a more pronounced difference observed in the upper half of the vessel, where the draft tube was implemented. On average, within the main body of the vessel (above the nozzle and below the filter), the RMS velocity and turbulent kinetic energy are 52% and 29% higher, respectively, in the original design compared to the improved design. In the region above $Z/D_o = 4$, the original design exhibits significantly higher RMS velocity and turbulent kinetic energy values than the improved design. This distinction arises from the absence of a draft tube in the original design, which cannot separate the central backflow from the outer upward jet. The particles sink under the influence of gravity from the middle of the annular filter, and then the downward solid–liquid suspension flow directly encounters the outer jet, which has opposite axial velocities and a considerable tangential velocity disparity. The interaction between these opposing flows generates bidirectional shear flows, leading to pronounced velocity fluctuations and a diminished average velocity within the outer upward jet. In addition, in the improved design, as the solid–liquid suspension descends out of the draft tube, it encounters the swirling jet, generating a shear flow characterized by increased velocity fluctuations. In the region below $Z/D_o = 2$, the disparity between the RMS velocity and kinetic energy of the mass flow in the improved design and the original design is comparatively minimal.

In conclusion, the incorporation of a central draft tube in the improved design led to a substantial augmentation in the magnitude of axial velocity in the outer region of the reactor. This enhancement corresponds to an increased velocity or frequency of particles circulating in the axial direction. Additionally, the rotational speed and average fluctuation velocity within the vessel decreased. Furthermore, the presence of the draft tube guarantees the involvement of a majority of particles in the circulation process. Consequently, these particles reach the region of high fluctuation velocity located in front of the nozzle. In this zone, characterized by elevated turbulence intensity, effective mixing of the solid–liquid suspension occurs, thereby facilitating enhanced reaction kinetics. Hence, the utilization of the draft tube not only ensures the presence of an adequate fluctuating velocity strength but also contributes to the enhancement of axial uniformity in the distribution of particles within the vessel.

7. Large scale flow structures in the reactor

As elucidated above, the RMS velocity in the nozzle and inlet tube at $Z/D_o \leq -0.5$ exhibits identical intensity and distribution as the original design. This can be inferred that the large-scale coherent structure present at the nozzle in the improved design likely bears similarities to the original design in terms of both strength and structure. Also, it is important to note that this particular region corresponds to the highest levels of fluctuating velocities within the vessel. Consequently, the analysis of the large-scale flow structure focuses primarily on the proximity of the nozzle area.

7.1. Temporal power spectrum analysis

To detect the frequency of the large-scale flow structures in the improved SFR, a temporal dataset encompassing a duration of 0.5 s is recorded. This dataset consists of the three velocity components of the liquid phase, acquired at a sampling frequency of 2000 Hz. The temporal power spectrum analysis was applied to a point in the stepped nozzle in a region with large velocity fluctuations. Fig. 10a illustrates the temporal fluctuations in velocities, where the red dashed line represents zero values. The fluctuations observed in these variables

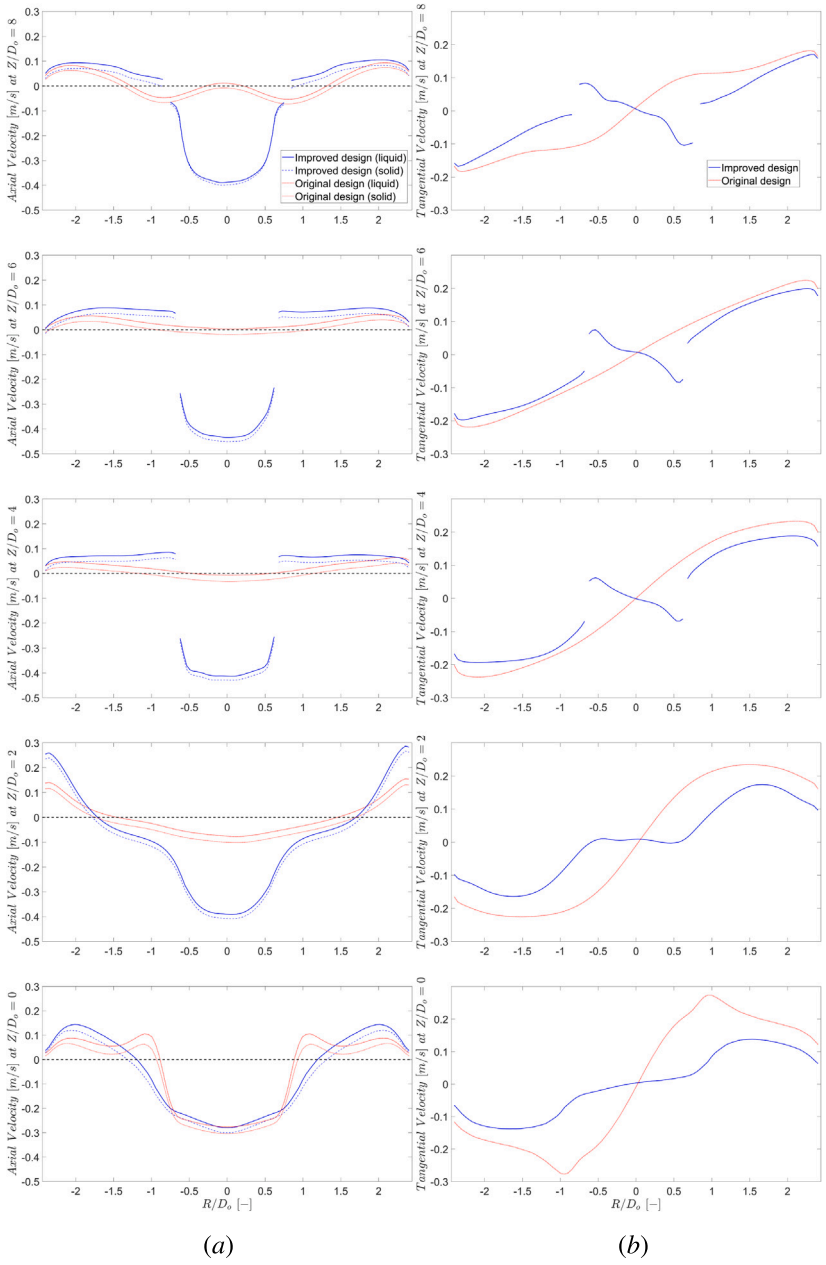

Fig. 8. Time-averaged axial velocity profiles of liquid and solid phase at $Z/D_o = 0, 2, 4, 6, 8$, from bottom to top, (*a*) axial velocity profiles of liquid and solid phase; (*b*) tangential velocity profiles.

exhibit distinct periodic variations with minimal interference from turbulent noise, as in the RANS model, the representation of small-scale turbulence fluctuations is predominantly based on the turbulent kinetic energy and turbulent dissipation rate. Furthermore, Fig. 10b presents the spectral analysis results of these variables. The first two peaks show a distinct intensity with frequencies of $f = 35.3$ Hz and $f = 70$ Hz, corresponding to a Strouhal number $St = fD_o/u_o$ of around 1 and 2. The first peak with Strouhal number 1 is consistent with other studies (Syred, 2006; Yang et al., 2023a). This bears resemblance to the frequencies associated with the double helical Precessing Vortex Core (PVC) and its second harmonic identified in the original design, connecting the improved and the original design in terms of flow characteristics and the precessing of coherent flow structures.

7.2. Spectral proper orthogonal decomposition

To study the large scale coherent structures in the nozzle, Spectral Proper Orthogonal Decomposition (SPOD) was applied to the liquid flow field. The effectiveness of this technique for swirling jet flows is shown in the studies of Vanierschot et al. (2020) and Zhang and Vanierschot (2021). The recorded velocity vector $U(x,t) = (u, v, w)$ is decomposed into a mean and fluctuation part,

$$U(x,t) = \bar{U}(x,t) + U^{\S}(x,t) = \bar{U}(x,t) + U^{\dagger}(x,t) + U^{\ddagger}(x,t). \quad (15)$$

The fluctuation part $U^{\S}(x,t)$ contains the coherent motion $U^{\dagger}(x,t)$ and the turbulent motion $U^{\ddagger}(x,t)$. Here, the turbulent part is only partial as due to the use of the $RNG\ k-\varepsilon$ model, a majority of the turbulence is contained in the turbulent energy k. The SPOD

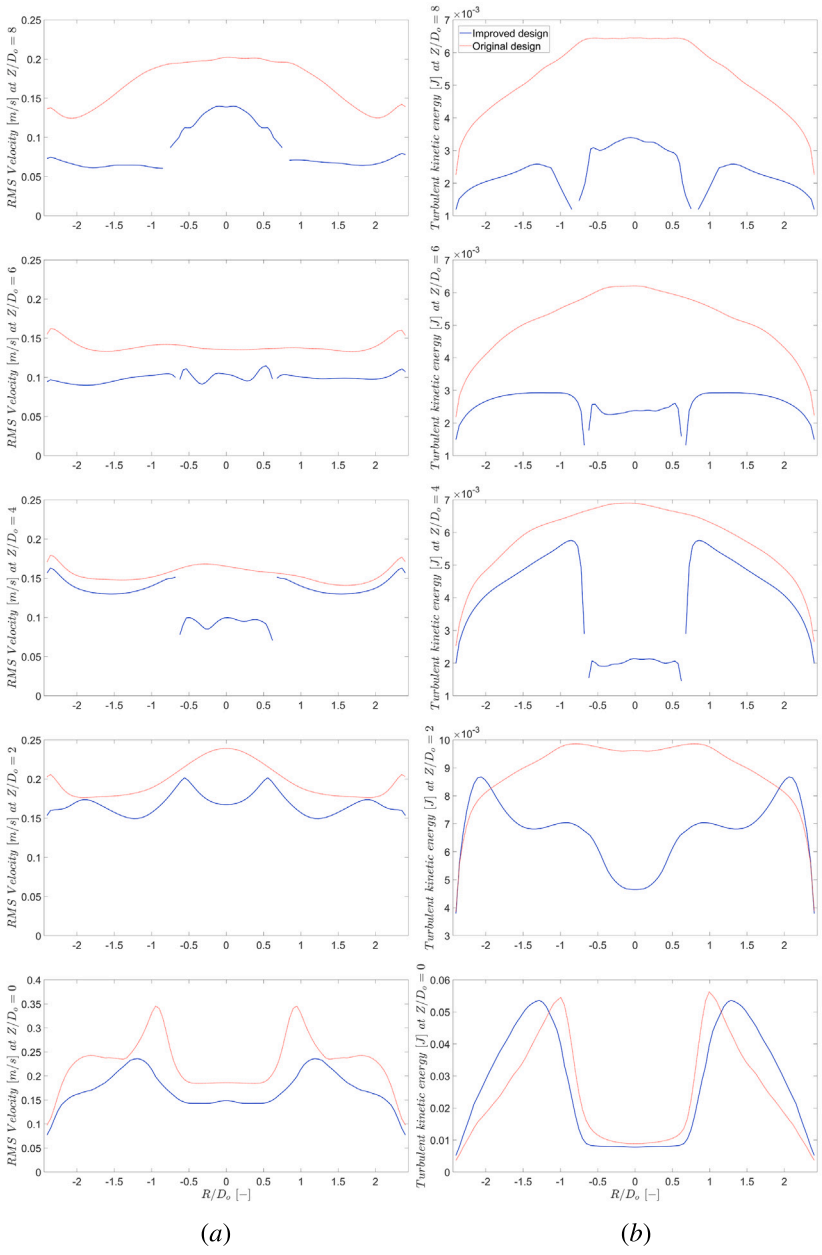

Fig. 9. (*a*) root mean square (RMS) profiles of liquid phase at Z/D_o = 0, 2, 4, 6, 8, from bottom to top, respectively; (*b*) turbulent kinetic energy profiles of liquid phase at Z/D_o = 0, 2, 4, 6, 8, from bottom to top, respectively. Both the original and the improved design are shown in red and blue, respectively.

approach allows detection of the coherent structures both in spatial and in frequency domains, especially when the flow dynamics are rather complicated (Sieber et al., 2016). The formulation of the SPOD technique is given as follows:

$$U(x,t) = \bar{U}(x,t) + \sum_{i=1}^{N} a_i(t)\boldsymbol{\Phi}_i(x), \tag{16}$$

in which the unsteady component is split into a collection of spatial modes $\boldsymbol{\Phi}_i(x)$ and associated temporal coefficients $a_i(t)$. Further details on SPOD can be found in Sieber's study (Sieber et al., 2016). In this study, a total of 800 snapshots of instantaneous velocity fields are recorded at a fixed frequency of 2000 Hz for the analysis. These snapshots are utilized to extract the SPOD mode pairs. Fig. 11 shows the SPOD spectrum, which provides insights into the frequency and energy content of the extracted mode pairs. The figure's vertical coordinates represent each mode pair's energy proportion to the total energy of the fluctuating velocity. The recorded velocity fields include large-scale structures and relatively larger-scale turbulence, while small-scale turbulence is contained in the turbulent kinetic energy (k) of the RANS model. Each dot in the figure corresponds to one mode pair, with the size and color indicating the magnitude of the correlation between the linked modes (Sieber et al., 2016). Mode pairs 1 and 2 have frequencies of 35.8 Hz and 71 Hz, corresponding to St = 1 and 2, respectively, which is consistent with the power spectrum analysis. These modes correspond to the Precessing Vortex Core (PVC), which is also found in the original design. In addition, these two mode pairs have a dominant energy content of 70.8% and 12.4%, respectively. The mode pairs extracted in the improved design have similar frequency and energy contributions compared to the original design. In addition, the temporal coefficients of mode pair 1 and 2 in the improved design exhibit a parallel evolution to those of the original design, demonstrating congruence in terms of magnitude, frequency, and phase shift. This consistency also extends to the spatial structure of both mode pairs, wherein the

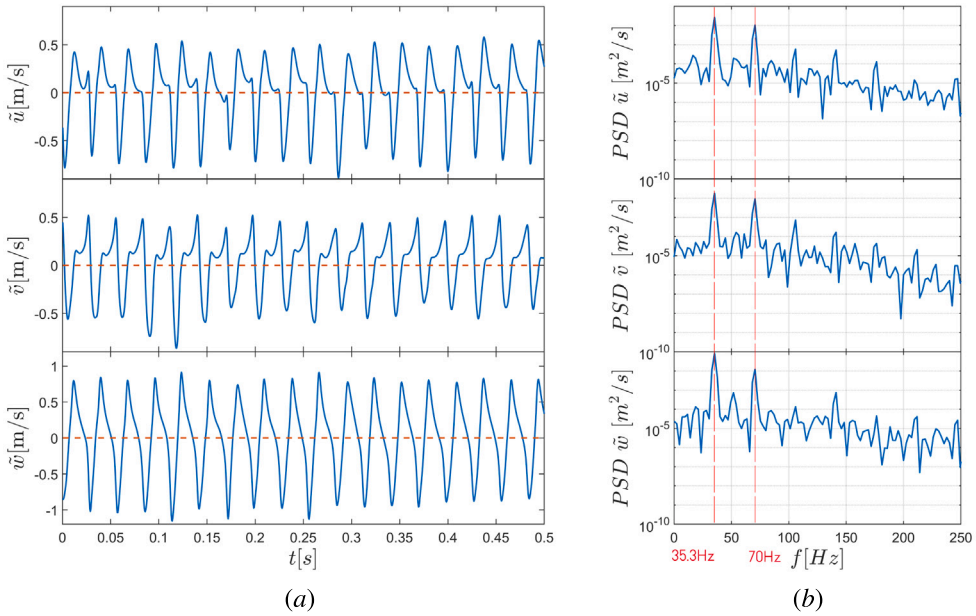

Fig. 10. Variable sampling at a location of high fluctuations in the reactor: (*a*) the sampled velocity components; (*b*) the corresponding power spectral density distribution (PSD). The red dashed lines indicate two main peaks in the PSD distributions with a frequency of 35.3 Hz and 70 Hz.

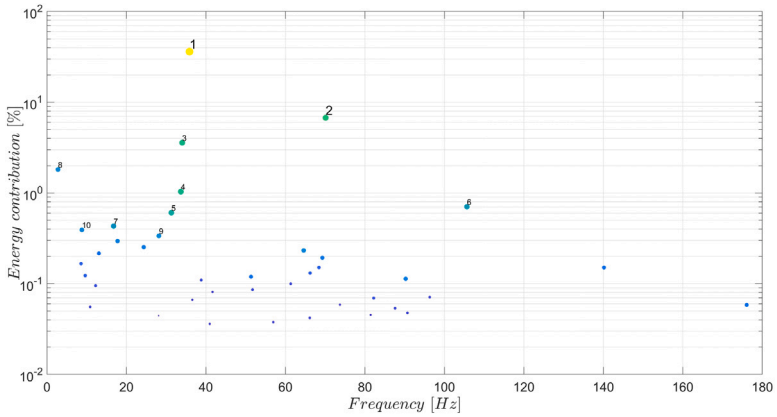

Fig. 11. The identified SPOD mode pairs and their percentage energy content.

extracted mode pairs from both designs manifest equivalent velocity intensity, distribution, and phase shift between the modes within each pair. Taking into account that the design's improvement is in the vessel's upper and middle regions, with a main impact on the flow pattern in the region above $Z/D_o = 2$, the nozzle and the area near the bottom are relatively less affected. Therefore, the mode pairs extracted from the improved design represent the same flow structure, dynamics, and harmonic correlations as the Precessing Vortex Core (PVC) found in the original design.

7.3. SPOD reconstruction and flow dynamics

To examine the dynamics of the coherent structures in the improved design, the investigated mode pairs are used to obtain $U^{\dagger}(x,t)$ in Eq. (15), which is added to the time-averaged velocity field $\bar{U}(x,t)$ to reconstruct the PVC structure. Figs. 12a and b show the reconstructed flow fields from mode pairs 1 and 2, respectively. To identify the vortex cores within these structures, the Q-criterion is utilized. The visualization of the vortex cores is achieved by representing an iso-surface of $Q = 6\times10^3\ 1/s^2$, where Q is defined as $Q = \left(|W|^2 - |S|^2\right)/2$, with W denoting the vorticity tensor and S representing the rate of strain. In a broader perspective, both mode pair 1 and mode pair 2 exhibit similar structural characteristics to the Precessing Vortex Core (PVC) identified in the original design. However, the detail of the structure differs in the conical nozzle. As the vortex core has a relatively low pressure, an iso-surface of pressure from an instant flow field can help to verify the presence of the PVC. Fig. 13 shows the structures obtained from the instantaneous pressure field by an iso-surface of $P = -70$ Pa. In the improved design, the low-pressure regions created by the two helical PVCs of the double-layer precessing structure are merged together. This is because the inner PVC is compressed by the solid–liquid suspension flow sinking through the draft tube. In Fig. 14a, the contours of the mean solid volume fraction reveal a notable region of high particle concentration in the conical nozzle (just below $Z/D_o = 0$). Note that the scale has been appropriately adjusted to accentuate this specific region with increased particle density. Higher particle concentrations result in a higher viscosity of the solid–liquid suspension, which has a large influence on the flow. In addition, Fig. 14b shows a snapshot of the transient iso-surface of solid volume fraction equal to 30%. The

(a) (b)

Fig. 12. The reconstructed PVC identified by the iso-surface of positive $Q = 6 \times 10^3$ 1/s: (*a*) two layer double helical PVC of mode pair 1; (*b*) two layer quadruple helical PVC of mode pair 2.

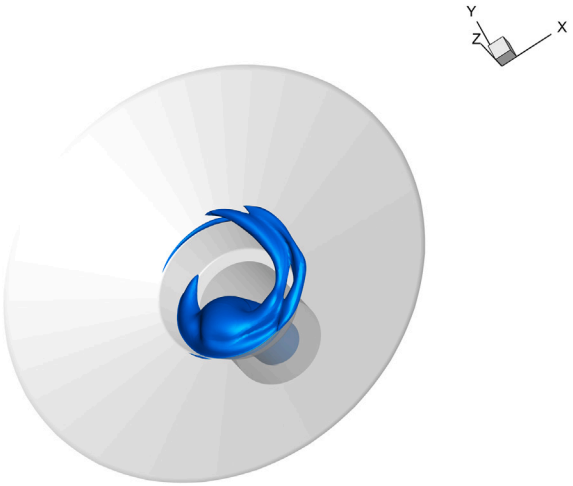

Fig. 13. Helical structures obtained from the instantaneous pressure field by an iso-surface of $P = -70$ Pa.

solid–liquid suspension with high concentration flows into the nozzle as a spiral structure, where it is dispersed by the high-velocity fluctuations of the PVC and eventually disappears.

The influence on the solid–liquid dispersion between the jet and PVC is mutual. Figs. 15a and b show the PVC of the improved design and original design, respectively. The contour in Fig. 15a represents the time-averaged solid volume fraction during a sampling time of 0.5s, used in the SPOD analysis. As the sinking particles were dispersed in the upper region of the vessel in the original design, the concentration of particles at the bottom of the vessel was lower, and there was no high concentration of solid–liquid suspension descending. The progression of the PVC in the original design was less affected. Comparing the structure of the PVC of both designs, the height of the PVC under high solid–liquid suspension compression is lower in the improved design than in the original one, and the distance between the two PVCs in the double-layer precessing structure is reduced. This causes the low-pressure region formed by these two vortex cores to merge, which is illustrated in Fig. 13. The proximity of these two PVCs also leads to the merging of the PCVs in the second-order harmonic structure of the improved design. This prevents the clear visualization of the extracted structure of the double-layer quadruple helix, as the merged helical inner PVC in Fig. 12b.

8. Conclusions

In this study, the mixing mechanisms and performance of an improved solid–liquid Swirl Flow Reactor (SFR) were analyzed using CFD, focusing on analyzing the principles of performance improvement by comparing the flow structure of the modified design phase with that of the original design. The simulation is applied to a case with the same Reynolds number $Re = 130.000$ and swirl number $Sw^* = 1.7$ as the original design, discussed in the study of Yang et al. (2023a). The SFR was simulated using the EE-KTGF model coupled with the Renormalization Group (RNG) $k - \varepsilon$ turbulence model. The utilization

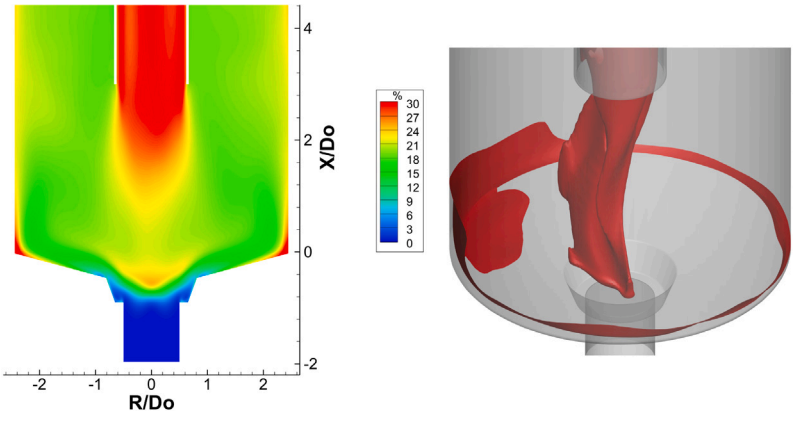

(a) (b)

Fig. 14. (*a*) Time-averaged particle volume fraction field in a plane tilted 45 degrees in the azimuthal direction; (*b*) instantaneous iso-surface of solid volume fraction equal to 30%.

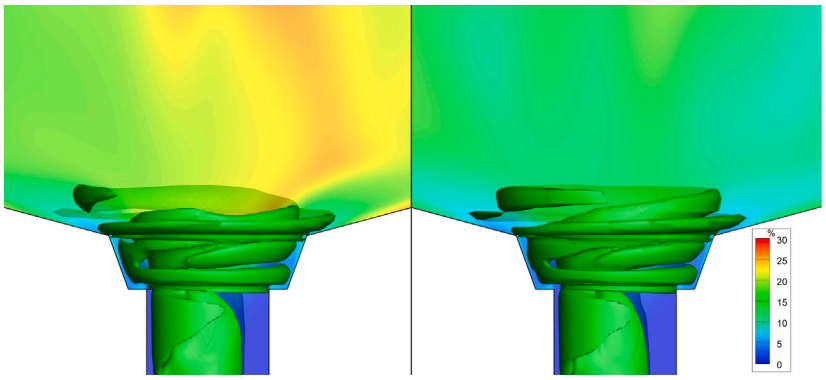

(a) (b)

Fig. 15. The reconstructed PVC identified by the iso-surface of positive $Q = 6 \times 10^3$ 1/s, and the slices show the contours of time-averaged particle volume fraction: (*a*) double layer helical PVC of mode pair 1 in improved design; (*b*) double layer helical PVC of mode pair 1 in original design.

of this model for multi-phase mixing problems characterized by high particle concentrations has been extensively validated and established as reliable in numerous studies focusing on solid–liquid mixing tanks. The improved SFR exhibits a more homogeneous mixing performance, with a homogeneity of 0.991 compared to 0.945 in the original design. The additional draft tube separates the inner and outer flows as expected and improves the axial distribution of the particles, and it also leads to a reduction in the average fluctuation of velocity within the vessel. However, guided by the draft tube, most particles are able to flow back from the outlet side back to the nozzle, where considerable velocity fluctuations and turbulence are still retained, which facilitates the solid–liquid mixing. In addition, the improved design also exhibits the presence of the flattened double-layer helical precessing vortex core (PVC) and its second-order harmonic, similar to those observed in the original design. Both designs have identical spatial structures, precessing frequencies, and contributions to the fluctuating velocity kinetic energy. The PVC present in the Coanda jet plays a crucial role in generating strong fluctuations and facilitating the rapid dispersion of the dense particle sinking stream, which becomes highly concentrated as a result of the draft tube. Furthermore, the high-concentration downward flow leads to the compression of the PVC and the merging of the low-pressure zone within the vortex core.

CRediT authorship contribution statement

Zhu Yang: Conceptualization, Data curation, Formal analysis, Investigation, Methodology, Software, Writing – original draft. **Thomas Holemans:** Conceptualization, Methodology, Writing – review & editing. **Bert Lagrain:** Conceptualization, Funding acquisition, Supervision, Writing – review & editing. **Bert Sels:** Conceptualization, Funding acquisition, Supervision, Writing – review & editing. **Maarten Vanierschot:** Conceptualization, Funding acquisition, Investigation, Software, Supervision, Writing – review & editing.

Declaration of competing interest

The authors declare that they have no known competing financial interests or personal relationships that could have appeared to influence the work reported in this paper.

Acknowledgments

The funding of this research by the 'Dienst onderzoekscoördinatie (DOC) KU Leuven' through grant number C3/19/015 is gratefully acknowledged. The computational resources and services used in this work were provided by the VSC (Flemish Supercomputer Center), funded by the Research Foundation - Flanders (FWO) and the Flemish Government – department EWI.

References

Ansys, 2019. ANSYS Fluent Theory Guide, Release 19.1. Ansys Inc.

Cao, G., Wang, Y., 2011. Nanostructures and nanomaterials: Synthesis, properties, and applications. In: World Scientific Series in Nanoscience and Nanotechnology, World Scientific.

Carletti, C., Montante, G., Westerlund, T., Paglianti, A., 2014. Analysis of solid concentration distribution in dense solid–liquid stirred tanks by electrical resistance tomography. Chem. Eng. Sci. 119, 53–64. http://dx.doi.org/10.1016/j.ces.2014.07.049, URL https://www.sciencedirect.com/science/article/pii/S0009250914003947.

Chen, S.H., Li, X.-F., 2020. Effects of particle concentration and physical properties on the apparent viscosity of a suspension of monodisperse concentric core–shell particles. Eur. J. Mech. B Fluids 84, 542–552. http://dx.doi.org/10.1016/j.euromechflu.2020.06.013, URL https://www.sciencedirect.com/science/article/pii/S0997754619306387.

Coker, A.K., 2007. 7 - mixing of liquids. In: Coker, A.K. (Ed.), Ludwig's Applied Process Design for Chemical and Petrochemical Plants, Fourth Ed. Gulf Professional Publishing, pp. 445–523. http://dx.doi.org/10.1016/B978-075067766-0/50014-2, URL https://www.sciencedirect.com/science/article/pii/B9780750677660500142.

Cooreman, E., Vangeel, T., Van Aelst, K., Van Aelst, J., Lauwaert, J., Thybaut, J.W., Van den Bosch, S., Sels, B.F., 2020. Perspective on overcoming scale-up hurdles for the reductive catalytic fractionation of lignocellulose biomass. Ind. Eng. Chem. Res. 59 (39), 17035–17045. http://dx.doi.org/10.1021/acs.iecr.0c02294.

Dang, X., Guo, J., Yang, L., Xue, S., Ai, B., Li, X., Chen, L., Li, W., Qin, H., Zhang, J., 2022. Effects of blade structures on the dissolution and gas-liquid mass transfer performance of cup-shaped blade mixers. J. Taiwan Inst. Chem. Eng. 131, 104149. http://dx.doi.org/10.1016/j.jtice.2021.11.016, URL https://www.sciencedirect.com/science/article/pii/S1876107021006453.

Drago, J., Tones, M., 2009. Understanding sealing solutions. Chem. Eng. Progr. 105 (7), 58–63.

Fotovati, S., Tafreshi, H.V., Pourdeyhimi, B., 2012. A macroscale model for simulating pressure drop and collection efficiency of pleated filters over time. Sep. Purif. Technol. 98, 344–355. http://dx.doi.org/10.1016/j.seppur.2012.07.009, URL https://www.sciencedirect.com/science/article/pii/S1383586612003826.

Fratczak, J., Hidalgo Herrador, J.M., Lederer, J., Stevens, L., Uguna, C., Snape, C., Gómez de la Fuente, J.L., Anděl, L., Svoboda, P., Pinto, F., 2018. Direct primary brown coal liquefaction via non-catalytic and catalytic co-processing with model, waste and petroleum-derived hydrogen donors. Fuel 234, 364–370. http://dx.doi.org/10.1016/j.fuel.2018.06.131, URL https://www.sciencedirect.com/science/article/pii/S0016236118311839.

Gidaspow, D., 1994. Multiphase Flow and Fluidization: Continuum and Kinetic Theory Descriptions. Academic Press, Google-Books-ID: DTAFZ9rIfQwC.

Gu, D., Liu, Z., Xie, Z., Li, J., Tao, C., Wang, Y., 2017. Numerical simulation of solid-liquid suspension in a stirred tank with a dual punched rigid-flexible impeller. Adv. Powder Technol. 28 (10), 2723–2734. http://dx.doi.org/10.1016/j.apt.2017.07.025, URL https://www.sciencedirect.com/science/article/pii/S0921883117303102.

Gupta, A.K., Lilley, D.G., Syred, N., 1984. Swirl flows. In: Energy and engineering science series, Abacus Press, Tunbridge Wells, Kent, OCLC: 11971811.

Gyllenram, W., Nilsson, H., Davidson, L., 2006. Large eddy simulation of turbulent swirling flow through a sudden expansion. In: Proceedings of the 23rd IHAR Synposium. Yokohama, pp. 1–10.

Hinze, J.O., 1975. Turbulence. McGraw-Hill Publishing Co, New York.

Hoekman, S.K., Broch, A., Robbins, C., 2011. Hydrothermal carbonization (HTC) of lignocellulosic biomass. Energy Fuels 25 (4), 1802–1810. http://dx.doi.org/10.1021/ef101745n, Publisher: American Chemical Society.

Hrouda, A., Capek, L., Vanierschot, M., Denis, K., 2021. Macroscale simulation of the filtration process of porous media based on statistical capturing models. Sep. Purif. Technol. 266, 118577. http://dx.doi.org/10.1016/j.seppur.2021.118577, URL https://www.sciencedirect.com/science/article/pii/S138358662100277X.

Huilin, L., Gidaspow, D., 2003. Hydrodynamics of binary fluidization in a riser: CFD simulation using two granular temperatures. Chem. Eng. Sci. 58 (16), 3777–3792. http://dx.doi.org/10.1016/S0009-2509(03)00238-0, URL https://www.sciencedirect.com/science/article/pii/S0009250903002380.

Jaszczur, M., Młynarczykowska, A., 2020. A general review of the current development of mechanically agitated vessels. Processes 8 (8), http://dx.doi.org/10.3390/pr8080982, URL https://www.mdpi.com/2227-9717/8/8/982.

Kasat, G.R., Khopkar, A.R., Ranade, V.V., Pandit, A.B., 2008. CFD simulation of liquid-phase mixing in solid–liquid stirred reactor. Chem. Eng. Sci. 63 (15), 3877–3885. http://dx.doi.org/10.1016/j.ces.2008.04.018, URL https://www.sciencedirect.com/science/article/pii/S0009250908001929.

Kazemzadeh, A., Ein-Mozaffari, F., Lohi, A., 2020. Effect of impeller type on mixing of highly concentrated slurries of large particles. Particuology 50, 88–99. http://dx.doi.org/10.1016/j.partic.2019.07.004, URL https://www.sciencedirect.com/science/article/pii/S1674200119301166.

Kuzmin, A.O., 2021. Confined multiphase swirled flows in chemical engineering. Rev. Chem. Eng. 37 (1), 31–68. http://dx.doi.org/10.1515/revce-2019-0019, URL https://www.degruyter.com/document/doi/10.1515/revce-2019-0019/html?lang=en. Publisher: De Gruyter.

Launder, B.E., Spalding, D.B., 1974. The numerical computation of turbulent flows. Comput. Methods Appl. Mech. Engrg. 3 (2), 269–289. http://dx.doi.org/10.1016/0045-7825(74)90029-2, URL https://www.sciencedirect.com/science/article/pii/0045782574900292.

Li, J., Deng, B., Zhang, B., Shen, X., Kim, C.N., 2015. CFD simulation of an unbaffled stirred tank reactor driven by a magnetic rod: Assessment of turbulence models. Water Sci. Technol. 72 (8), 1308–1318. http://dx.doi.org/10.2166/wst.2015.314, URL https://iwaponline.com/wst/article/72/8/1308/19093/CFD-simulation-of-an-unbaffled-stirred-tank. Publisher: IWA Publishing.

Liu, F., Lu, T., Li, K., Xie, C., Zhao, H., 2023. Computational fluid dynamics study on the effect of stirring parameters on solid–liquid suspension in the slurry electrolysis square tank. Adv. Powder Technol. 34 (5), 104016. http://dx.doi.org/10.1016/j.apt.2023.104016, URL https://www.sciencedirect.com/science/article/pii/S0921883123000791.

Liu, B., Sun, N., Jin, Z., Zhang, Y., Sunden, B., 2019. Numerical investigation and estimating correlation of micromixing performance of coaxial mixers. Ind. Eng. Chem. Res. 58 (49), 22376–22388. http://dx.doi.org/10.1021/acs.iecr.9b04406, URL https://doi.org/10.1021/acs.iecr.9b04406. Publisher: American Chemical Society.

Maluta, F., Paglianti, A., Montante, G., 2019. RANS-based predictions of dense solid–liquid suspensions in turbulent stirred tanks. Chem. Eng. Res. Des. 147, 470–482. http://dx.doi.org/10.1016/j.cherd.2019.05.015, URL https://www.sciencedirect.com/science/article/pii/S0263876219302254.

Min, J., Gao, Z., 2006. Large eddy simulations of mixing time in a stirred tank. Chin. J. Chem. Eng. 14 (1), 1–7. http://dx.doi.org/10.1016/S1004-9541(06)60030-X, URL https://www.sciencedirect.com/science/article/pii/S100495410660030X.

Mishra, P., Ein-Mozaffari, F., 2017. Using computational fluid dynamics to analyze the performance of the maxblend impeller in solid-liquid mixing operations. Int. J. Multiph. Flow 91, 194–207. http://dx.doi.org/10.1016/j.ijmultiphaseflow.2017.01.009, URL https://www.sciencedirect.com/science/article/pii/S030193221630413X.

Montante, G., Magelli, F., 2007. Mixed solids distribution in stirred vessels: Experiments and computational fluid dynamics simulations. Ind. Eng. Chem. Res. 46 (9), 2885–2891. http://dx.doi.org/10.1021/ie060616i, Publisher: American Chemical Society.

Ogus, G., Baelmans, M., Lammertyn, J., Vanierschot, M., 2018. Numerical investigation of a novel microscale swirling jet reactor for medical sensor applications. J. Phys. Conf. Ser. 980 (1), 012030. http://dx.doi.org/10.1088/1742-6596/980/1/012030, Publisher: IOP Publishing.

Pangarkar, V.G., 2017. Process intensification in multiphase reactors: From concept to reality. Chem. Eng. Process. - Process Intensif. 120, 1–8. http://dx.doi.org/10.1016/j.cep.2017.06.004, URL https://www.sciencedirect.com/science/article/pii/S0255270117302830.

Peker, S.M., Helvaci, S.S., 2008. Solid-liquid Two Phase Flow. Elsevier.

Poelma, C., 2016. Ultrasound imaging velocimetry: A review. Exp. Fluids 58 (1), 3. http://dx.doi.org/10.1007/s00348-016-2283-9.

Raffel, M., Willert, C.E., Scarano, F., Kähler, C.J., Wereley, S.T., Kompenhans, J., 2018. Physical and technical background. In: Raffel, M., Willert, C.E., Scarano, F., Kähler, C.J., Wereley, S.T., Kompenhans, J. (Eds.), Particle Image Velocimetry: A Practical Guide. Springer International Publishing, Cham, pp. 33–111. http://dx.doi.org/10.1007/978-3-319-68852-7_2.

Renders, T., Van den Bossche, G., Vangeel, T., Van Aelst, K., Sels, B., 2019. Reductive catalytic fractionation: state of the art of the lignin-first biorefinery. Curr. Opin. Biotechnol. 56, 193–201. http://dx.doi.org/10.1016/j.copbio.2018.12.005, URL https://www.sciencedirect.com/science/article/pii/S0958166918301678.

Renders, T., Cooreman, E., Van den Bosch, S., Schutyser, W., Koelewijn, S.-F., Vangeel, T., Deneyer, A., Van den Bossche, G., Courtin, C.M., Sels, B.F., 2018. Catalytic lignocellulose biorefining in n-butanol/water: a one-pot approach toward phenolics, polyols, and cellulose. Green Chem. 20 (20), 4607–4619. http://dx.doi.org/10.1039/C8GC01031E, Publisher: The Royal Society of Chemistry.

Sardeshpande, M.V., Juvekar, V.A., Ranade, V.V., 2011. Solid suspension in stirred tanks: UVP measurements and CFD simulations. Can. J. Chem. Eng. 89 (5), 1112–1121. http://dx.doi.org/10.1002/cjce.20548, URL http://onlinelibrary.wiley.com/doi/abs/10.1002/cjce.20548.

Shah, Y.T., 1991. Design parameters for mechanically agitated reactors. In: Wei, J., Anderson, J.L., Bischoff, K.B., Seinfeld, J.H. (Eds.), Advances in Chemical Engineering. vol. 17. Academic Press, pp. 1–206. http://dx.doi.org/10.1016/S0065-2377(08)60115-5, URL https://www.sciencedirect.com/science/article/pii/S0065237708601155.

Shi, P., Rzehak, R., 2020. Solid-liquid flow in stirred tanks: Euler-Euler/RANS modeling. Chem. Eng. Sci. 227, 115875. http://dx.doi.org/10.1016/j.ces.2020.115875, URL https://www.sciencedirect.com/science/article/pii/S0009250920304073.

Shih, T.-H., Liou, W.W., Shabbir, A., Yang, Z., Zhu, J., 1995. A new k-ϵ eddy viscosity model for high Reynolds number turbulent flows. Comput. & Fluids 24 (3), 227–238. http://dx.doi.org/10.1016/0045-7930(94)00032-T, URL https://www.sciencedirect.com/science/article/pii/004579309400032T.

Shukla, A., Prakash, A., 2006. Ultrasonic technique to determine particle size and concentration in slurry systems. Chem. Eng. Sci. 61 (8), 2468–2475. http://dx.doi.org/10.1016/j.ces.2005.11.027, URL https://www.sciencedirect.com/science/article/pii/S0009250905008778.

Sieber, M., Paschereit, C.O., Oberleithner, K., 2016. Spectral proper orthogonal decomposition. J. Fluid Mech. 792, 798–828. http://dx.doi.org/10.1017/jfm.2016.103.

Syred, N., 2006. A review of oscillation mechanisms and the role of the precessing vortex core (PVC) in swirl combustion systems. Prog. Energy Combust. Sci. 32 (2), 93–161. http://dx.doi.org/10.1016/j.pecs.2005.10.002, URL https://www.sciencedirect.com/science/article/pii/S0360128505000353.

Tamburini, A., Cipollina, A., Micale, G., Brucato, A., Ciofalo, M., 2014. Influence of drag and turbulence modelling on CFD predictions of solid liquid suspensions in stirred vessels. Chem. Eng. Res. Des. 92 (6), 1045–1063. http://dx.doi.org/10.1016/j.cherd.2013.10.020, URL https://www.sciencedirect.com/science/article/pii/S0263876213004401.

Tschulkow, M., Compernolle, T., Van den Bosch, S., Van Aelst, J., Storms, I., Van Dael, M., Van den Bossche, G., Sels, B., Van Passel, S., 2020. Integrated techno-economic assessment of a biorefinery process: The high-end valorization of the lignocellulosic fraction in wood streams. J. Clean. Prod. 266, 122022. http://dx.doi.org/10.1016/j.jclepro.2020.122022, URL https://www.sciencedirect.com/science/article/pii/S0959652620320692.

Van den Bosch, S., Schutyser, W., Vanholme, R., Driessen, T., Koelewijn, S.-F., Renders, T., Meester, B.D., Huijgen, W.J.J., Dehaen, W., Courtin, C.M., Lagrain, B., Boerjan, W., Sels, B.F., 2015. Reductive lignocellulose fractionation into soluble lignin-derived phenolic monomers and dimers and processable carbohydrate pulps. Energy Environ. Sci. 8 (6), 1748–1763. http://dx.doi.org/10.1039/C5EE00204D, URL https://pubs.rsc.org/en/content/articlelanding/2015/ee/c5ee00204d, Publisher: The Royal Society of Chemistry.

Vanierschot, M., Van den Bulck, E., 2007a. Influence of the nozzle geometry on the hysteresis of annular swirling jets. Combust. Sci. Technol. 179 (8), 1451–1466, Publisher: Taylor & Francis _eprint: https://doi.org/10.1080/00102200601147856.

Vanierschot, M., Van den Bulck, E., 2007b. Numerical study of hysteresis in annular swirling jets with a stepped-conical nozzle. Internat. J. Numer. Methods Fluids 54 (3), 313–324. http://dx.doi.org/10.1002/fld.1400, URL http://onlinelibrary.wiley.com/doi/abs/10.1002/fld.1400.

Vanierschot, M., Müller, J.S., Sieber, M., Percin, M., van Oudheusden, B.W., Oberleithner, K., 2020. Single- and double-helix vortex breakdown as two dominant global modes in turbulent swirling jet flow. J. Fluid Mech. 883, A31. http://dx.doi.org/10.1017/jfm.2019.872.

Wadnerkar, D., Tade, M.O., Pareek, V.K., Utikar, R.P., 2016. CFD simulation of solid–liquid stirred tanks for low to dense solid loading systems. Particuology 29, 16–33. http://dx.doi.org/10.1016/j.partic.2016.01.012, URL https://www.sciencedirect.com/science/article/pii/S1674200116300256.

Wadnerkar, D., Utikar, R.P., Tade, M.O., Pareek, V.K., 2012. CFD simulation of solid–liquid stirred tanks. Adv. Powder Technol. 23 (4), 445–453. http://dx.doi.org/10.1016/j.apt.2012.03.007, URL https://www.sciencedirect.com/science/article/pii/S0921883112000386.

Wang, S., Boger, D.V., Wu, J., 2012. Energy efficient solids suspension in an agitated vessel–water slurry. Chem. Eng. Sci. 74, 233–243. http://dx.doi.org/10.1016/j.ces.2012.02.035, URL https://www.sciencedirect.com/science/article/pii/S0009250912001315.

Wang, F., Mao, Z.-S., Wang, Y., Yang, C., 2006. Measurement of phase holdups in liquid–liquid–solid three-phase stirred tanks and CFD simulation. Chem. Eng. Sci. 61 (22), 7535–7550. http://dx.doi.org/10.1016/j.ces.2006.08.046, URL https://www.sciencedirect.com/science/article/pii/S000925090600532X.

Wang, L., Wang, M., Tian, Y., Qi, Y., Gao, Y., 2022. Experimental and simulation study on mixing time and suspension quality of liquid-solid flow field in stirred reactor with draft tube. Int. J. Chem. React. Eng. 20 (4), 445–463. http://dx.doi.

org/10.1515/ijcre-2021-0151, URL https://www.degruyter.com/document/doi/10.1515/ijcre-2021-0151/html. Publisher: De Gruyter.

Wiederseiner, S., Andreini, N., Epely-Chauvin, G., Ancey, C., 2011. Refractive-index and density matching in concentrated particle suspensions: A review. Exp. Fluids 50 (5), 1183–1206. http://dx.doi.org/10.1007/s00348-010-0996-8.

Wright, S.F., Zadrazil, I., Markides, C.N., 2017. A review of solid–fluid selection options for optical-based measurements in single-phase liquid, two-phase liquid–liquid and multiphase solid–liquid flows. Exp. Fluids 58 (9), 108. http://dx.doi.org/10.1007/s00348-017-2386-y.

Xiang, H.W., Laesecke, A., Huber, M.L., 2006. A new reference correlation for the viscosity of methanol. J. Phys. Chem. Ref. Data 35 (4), 1597–1620. http://dx.doi.org/10.1063/1.2360605.

Xie, L., Luo, Z.-H., 2018. Modeling and simulation of the influences of particle-particle interactions on dense solid–liquid suspensions in stirred vessels. Chem. Eng. Sci. 176, 439–453. http://dx.doi.org/10.1016/j.ces.2017.11.017, URL https://www.sciencedirect.com/science/article/pii/S0009250917306966.

Xu, Z., Yang, C., Zhang, Z., Liu, B., Jin, Z., 2021. Study on the numerical model of dense solid suspension driven by a coaxial mixer. Ind. Eng. Chem. Res. 60 (4), 1939–1951. http://dx.doi.org/10.1021/acs.iecr.0c06287, Publisher: American Chemical Society.

Yakhot, V., Orszag, S.A., 1986. Renormalization group analysis of turbulence. I. basic theory. J. Sci. Comput. 1 (1), 3–51. http://dx.doi.org/10.1007/BF01061452.

Yang, Z., 2023. Design and Optimization of a Swirling Flow Reactor for Solid-Liquid Mixing (Ph.D. thesis). KU Leuven, Leuven.

Yang, Z., Castaneda, V., Ogus, G., Holemans, T., Vanierschot, M., Valera-Medina, A., 2023a. Identification and dynamics of coherent structures in a Coanda swirling jet flow. Exp. Therm Fluid Sci. 142, 110817. http://dx.doi.org/10.1016/j.expthermflusci.2022.110817, URL https://www.sciencedirect.com/science/article/pii/S0894177722002138.

Yang, Z., Holemans, T., Lagrain, B., Sels, B., Vanierschot, M., 2023b. A solid-liquid mixing reactor based on swirling flow technology. Chem. Eng. Sci. 280, 119054. http://dx.doi.org/10.1016/j.ces.2023.119054, URL https://www.sciencedirect.com/science/article/pii/S0009250923006103.

Yang, C., Mao, Z.-S., 2014. Chapter 3 - multiphase stirred reactors. In: Yang, C., Mao, Z.-S. (Eds.), Numerical Simulation of Multiphase Reactors with Continuous Liquid Phase. Academic Press, Oxford, pp. 75–151. http://dx.doi.org/10.1016/B978-0-08-099919-7.00003-2, URL https://www.sciencedirect.com/science/article/pii/B9780080999197000032.

Yao, Y., Liu, Z., Zheng, G., Tao, C., Wang, Y., Xi, B., 2023. Intensification of solid–liquid suspension performance in an elliptical uncovered unbaffled stirred tank. Ind. Eng. Chem. Res. 62, 5315–5325.

Zhang, Y., Vanierschot, M., 2021. Determination of single and double helical structures in a swirling jet by spectral proper orthogonal decomposition. Phys. Fluids 33 (1), 015115. http://dx.doi.org/10.1063/5.0032985.